






Defect engineering on V_2O_3 cathode for long-cycling aqueous zinc metal batteries

Kefu Zhu^{1,7}, Shiqiang Wei^{1,7}, Hongwei Shou^{1,2,7}, Feiran Shen^{3,7}, Shuangming Chen¹ [✉], Pengjun Zhang¹, Changda Wang¹, Yuyang Cao¹, Xin Guo¹, Mi Luo⁴, Hongjun Zhang¹ ⁴, Bangjiao Ye⁴, Xiaojun Wu¹ ², Lunhua He^{3,5,6} [✉] & Li Song¹ [✉]

Defect engineering is a strategy that is attracting widespread attention for the possibility of modifying battery active materials in order to improve the cycling stability of the electrodes. However, accurate investigation and quantification of the effect of the defects on the electrochemical energy storage performance of the cell are not trivial tasks. Herein, we report the quantification of vanadium-defective clusters (i.e., up to 5.7%) in the V_2O_3 lattice via neutron and X-ray powder diffraction measurements, positron annihilation lifetime spectroscopy, and synchrotron-based X-ray analysis. When the vanadium-defective V_2O_3 is employed as cathode active material in an aqueous Zn coin cell configuration, capacity retention of about 81% after 30,000 cycles at 5 A g^{-1} is achieved. Density functional theory calculations indicate that the vanadium-defective clusters can provide favorable sites for reversible Zn-ion storage. Moreover, the vanadium-defective clusters allow the storage of Zn ions in V_2O_3 , which reduces the electrostatic interaction between the host material and the multivalent ions.

¹National Synchrotron Radiation Laboratory, CAS Center for Excellence in Nanoscience, University of Science and Technology of China, 230029 Hefei, China. ²School of Chemistry and Material Sciences, University of Science and Technology of China, 230026 Hefei, China. ³Spallation Neutron Source Science Center, 523803 Dongguan, China. ⁴State Key Laboratory of Particle Detection and Electronics & Hefei National Laboratory for Physical Sciences at the Microscale, University of Science and Technology of China, 230026 Hefei, China. ⁵Beijing National Laboratory for Condensed Matter Physics, Institute of Physics, Chinese Academy of Sciences, 100190 Beijing, China. ⁶Songshan Lake Materials Laboratory, 523808 Dongguan, China. ⁷These authors contributed equally: Kefu Zhu, Shiqiang Wei, Hongwei Shou, Feiran Shen. ✉email: csmp@ustc.edu.cn; lhhe@iphy.ac.cn; song2012@ustc.edu.cn

With the increase of energy crisis and environmental pollution problems, it is essential to develop green and clean energy storage devices. As a bellwether in the field of energy storage, lithium-ion batteries (LIBs) are a key electrochemical energy storage device^{1,2}. However, emerging worries are their limited lithium resources and hazard issues towards future large-scale applications^{3–6}. Encouragingly, rechargeable aqueous zinc-ion batteries (ZIBs) have emerged as the most promising complements to LIBs owing to the high theoretical specific capacity (820 mA h g⁻¹), low cost, abundant resources, and environmental friendliness^{7–9}. Aqueous ZIBs were first introduced by Kang et al.¹⁰. Afterward, Mn-based oxides¹¹, Prussian blue analogs¹², and V-based oxides were widely studied as potential aqueous ZIBs cathode materials. However, the structural instability of Mn-based oxides during cycling brings about poor stability and the low specific capacity (<100 mA h g⁻¹) of Prussian blue analogs, thus restricting its further development, while vanadium has a low price, rich crystal structure, abundant reserves, and multiple valence states, which makes its oxides have a higher specific capacity and better stability. However, significant upgrading is needed to widen its application. The search for long-cycling V-based oxides cathodes for aqueous ZIBs still remains one of the most compelling issues due to serious consequences of stability penalty caused by the aqueous system and bigger ionic radius of Zn²⁺. To promote the stability of electrodes, tremendous efforts have been devoted in the past few years. One common strategy used is defect engineering, in which the strong electrostatic interaction between the host and multivalent ions with a larger charge can be efficiently reduced. This can accelerate the reaction kinetics and facilitate the reversible storage of Zn ions^{13–16}. Particularly, the research of defects in oxide electrodes most used for ZIBs is desirable due to the complex composition and the dynamic process during the working process. Accurate quantification of material defects is essential to determine the metal vacancies and oxygen vacancies at the same time. However, it is extremely hard to simultaneously determine the concentration of such two vacancies. For example, Rietveld refinement of X-ray diffraction (XRD) measurements is commonly employed to quantify defect concentration. Nevertheless, light oxygen is difficult to be detected by XRD owing to its small atomic radius, compared with most metal elements. Rietveld refinement of neutron powder diffraction (NPD) measurements is also often performed to quantify defect concentration. However, the scattering factor of heavier elements is too small to be probed by the mean of NPD¹⁷. Consequently, the joint application of multiple spectroscopy is essential to accurately quantify defects.

In this work, we have quantified that vanadium defective-V₂O₃ (V_d-V₂O₃) electrode in aqueous ZIBs contains 5.7% V_d clusters by Rietveld refinement with combined XRD and NPD patterns. Notably, the V₂O₃ cathode containing V_d clusters can deliver long cycling stability (81% retention after 30,000 cycles at a specific current of 5 A g⁻¹). Accurately quantifying and identifying the effect of defects provide a better understanding to further rational design of cathodes with long stability for energy storage devices.

Results and Discussion

Structure and morphology characterization of V_d-V₂O₃. The V_d-V₂O₃ cathode was designed by a hydrothermal method and an ensuing annealing process (see Methods section for details). Scanning electron microscopy (SEM, Fig. 1a) and transmission electron microscope (TEM, Fig. 1b) images show that the V_d-V₂O₃ is a uniform multi-layer hierarchical structure assembled by thin nanosheets with a size of around 100–200 nm. In the high-resolution TEM (HRTEM, Fig. 1c) image of the V_d-V₂O₃, a

lattice fringe with a layer spacing of $d = 0.27$ nm was observed, corresponding to the (104) lattice plane. The surface area and pore size were detected by the physical adsorption method. The V_d-V₂O₃ exhibited a large local pore size of about 22 nm (Fig. 1d inset). According to the Brunauer-Emmett-Teller (BET) method, the V_d-V₂O₃ displayed a high surface area of 60.34 m² g⁻¹ (Fig. 1d), which can provide sufficient contact between the electrode and electrolyte and shorten the Zn²⁺ diffusion path time. The mesoporous structure (2–50 nm)¹⁸ is advantageous to the insertion and extraction of Zn²⁺, which can effectively improve the cycle life of the battery.

For detailed structure information, X-ray absorption fine structure (XAFS) measurements were carried out to investigate the local structure of V_d-V₂O₃. As illustrated in the XANES spectra of V K-edge (Fig. 2a), the absorption edge of the V_d-V₂O₃ is found to shift toward higher energy (Site B) compared with commercial V₂O₃ (c-V₂O₃), implying a higher average valence state in V_d-V₂O₃. The high-resolution X-ray photoelectron spectroscopy (XPS) measurements of V 2p further show that the valence states of V in both V_d-V₂O₃ and c-V₂O₃ are +3 and +4 coexistence (Supplementary Fig. 1). As comparison, the ratio of V⁴⁺ in V_d-V₂O₃ and c-V₂O₃ is 54.32% and 46.49% (Supplementary Table 1), indicating that the surface of V_d-V₂O₃ also processes a higher valence state. The identical result can be gotten from electron paramagnetic resonance (EPR) spectroscopy measurements, where the EPR signal of tetravalent vanadium has a stronger response strength^{19,20} (Supplementary Fig. 2). It has been reported that the surface of V₂O₃ is vulnerable to be oxidized to V⁴⁺, which explains the existence of V⁴⁺ in c-V₂O₃^{21,22}. But the situation in V_d-V₂O₃ is different, the surface of V_d-V₂O₃ is proved to be uniformly coated with carbon, which comes from the pyrolysis of organic substances such as urea in the raw material (Supplementary Figs. 3 and 4). Besides, Raman spectroscopy measurements further confirmed the presence of carbon in V_d-V₂O₃, but not in c-V₂O₃ (Supplementary Figure 5). Thermogravimetric analysis (TGA) shows that the carbon content is 22.92% (Supplementary Fig. 6). Surface coated with the carbon of V_d-V₂O₃ is believed to be not easily oxidized at room temperature²³, so the higher content of V⁴⁺ in V_d-V₂O₃ may attribute to the existence of vanadium vacancies, which leads to a valence increase of V. The pre-edge peak in the XANES of V K-edge corresponds to the electronic transition from 1s to 3d²⁴, which can promulgate the local structure symmetry. As shown in Fig. 2a (Site A), the increase of pre-edge peak intensity attributes to the decrease of local symmetry of V_d-V₂O₃. That is suggested that the structure of V_d-V₂O₃ is distorted around V atoms, owing to the absence of surrounding atoms. To further obtain the accurate coordination numbers (CN), the corresponding Fourier-transformed EXAFS is fitted as shown in Supplementary Fig. 7 and the detailed fitting results can be found in Supplementary Table 2. The results demonstrate that the CN of the V-V in V_d-V₂O₃ is significantly lower than that in c-V₂O₃ (2.2 vs. 4), confirming that there are vanadium vacancies in V_d-V₂O₃^{25–27}.

To further corroborate the defect situation in V_d-V₂O₃, we used positron annihilation lifetime spectroscopy (PALS) measurements to explore the defect type and concentration of the material²⁸. Table 1 shows the PALS results of V_d-V₂O₃ and c-V₂O₃. The PAL spectra are well decomposed into three life components (τ_1 , τ_2 , and τ_3). The shortest lifetime component (τ_1) corresponds to the positron annihilation in the defect-free bulk regions and tiny vacancies. The longer lifetime component (τ_2) is attributed to the positron annihilation in vacancy clusters or boundary regions. Combined with the following XRD and NPD refinement results, the τ_2 of c-V₂O₃ probably originates from positron annihilation in the boundary regions²⁹. The longest component (τ_3) of several nanoseconds often results from the

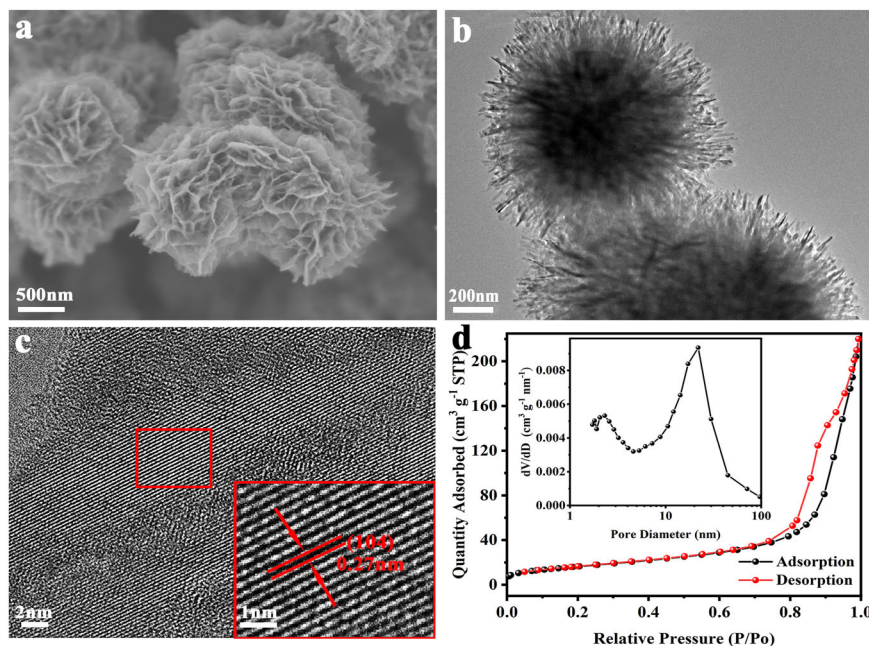


Fig. 1 Physicochemical characterization of $V_d-V_2O_3$. **a** SEM image. **b** TEM image. **c** HRTEM image. **d** Nitrogen adsorption and desorption isotherms. inset: pore size distribution.

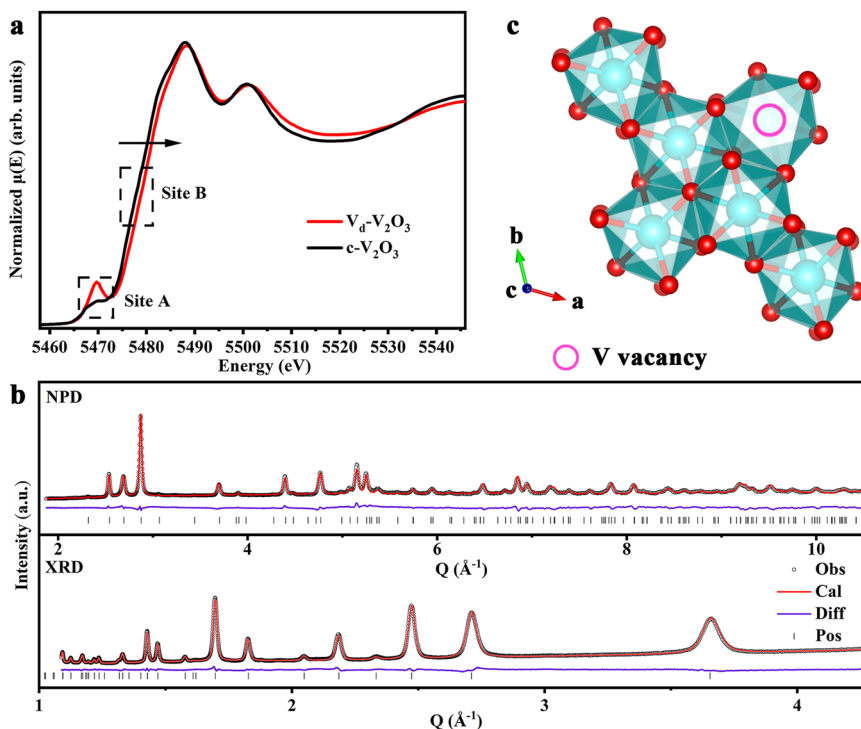


Fig. 2 Structural characterization of $V_d-V_2O_3$. **a** Normalized XANES spectra of V K-edge for $V_d-V_2O_3$ and $c-V_2O_3$. **b** Observed (black circle), calculated diffraction patterns (red line), their difference (purple line) and peak position (black bar) of the NPD pattern (upper part) and XRD pattern (lower part). **c** Schematic diagram of the structure of $V_d-V_2O_3$ along the c -axis. The oxygen atoms are represented by small red spheres, and the V atoms are depicted in blue.

Table 1 Position lifetime parameters of $V_d-V_2O_3$ and $c-V_2O_3$.

Sample	τ_1 (ps)	τ_2 (ps)	τ_3 (ns)	I_1 (%)	I_2 (%)	I_3 (%)
$V_d-V_2O_3$	156	373	1.559	17.02	78.01	4.97
$c-V_2O_3$	175	392	1.610	57.09	37.94	4.97

annihilation of ortho-positronium (boundary state of a positron and an electron, spin triplet) in some large voids which is the unoccupied space among close-packed nanograins. It is not correlated with the microstructure in nanograins^{30,31}, thus, we could neglect the longest component. The values of τ_1 (175 ps), τ_2 (392 ps), and τ_3 (1.610 ns) in $c-V_2O_3$ are very close to the previous results (171 ps, 414 ps, and 1.8 ns)³². For the $V_d-V_2O_3$

sample, the shortest lifetime component is lower than that of $c\text{-V}_2\text{O}_3$, indicating the significant existence of vacancy-type defects in $V_d\text{-V}_2\text{O}_3$, while large vacancy-type defects are not identified in $c\text{-V}_2\text{O}_3$. It is noteworthy that the intensity I_2 of τ_2 for $V_d\text{-V}_2\text{O}_3$ is 78.01%, further confirming that the concentration of vacancy clusters in $V_d\text{-V}_2\text{O}_3$ is much higher than that in $c\text{-V}_2\text{O}_3$. The PALS results provide reliable and valuable proof of the coexistence of vanadium vacancies with a relatively high concentration in $V_d\text{-V}_2\text{O}_3$, and the phenomenon of defect aggregation may occur.

To accurately determine the type and concentration of defects, we combined NPD and XRD techniques. In the $V_2\text{O}_3$ cathode, the neutron scattering amplitude of the V element is just -0.0382 cm^{-12} , and the atomic radius of the light oxygen element is $\sim 0.66\text{ \AA}$. As a result, the vanadium element in the $V_d\text{-V}_2\text{O}_3$ cathode is hard to be detected by NPD, while the light oxygen element is too small to be probed by XRD. However, the neutron scattering amplitude of the light oxygen element is as high as 0.5803 cm^{-12} , which is easy to be detected by NPD. The atomic radius of the vanadium element is 1.22 \AA , which is big enough to be probed by XRD. Therefore, Rietveld refinement with combined XRD and NPD patterns was conducted to reveal the crystal structure (Fig. 2b). The refinement results (Supplementary Table 3) show that the $V_d\text{-V}_2\text{O}_3$ has a typical corundum-type hexagonal structure (Space group: $R\bar{3}c$) with lattice parameters to be $a = b = 4.9473(1)\text{ \AA}$, $c = 13.9990(5)\text{ \AA}$. The V and O atoms occupy the 12c (0, 0, 0.15437(6)) and 18e (0.3145(3), 0, 0.25) crystallographic positions, respectively. Moreover, the occupancy rate of vanadium atoms at 12c sites is $\sim 94.3(1)\%$, while no oxygen vacancy was detected at 18e sites (Fig. 2c). In addition, the Rietveld analysis of $c\text{-V}_2\text{O}_3$ by combined XRD and NPD patterns also exhibits the crystal structure information as shown in Supplementary Fig. 8. Like $V_d\text{-V}_2\text{O}_3$, $c\text{-V}_2\text{O}_3$ belongs to the identical space group, with similar lattice parameters and the positions occupied by V and O atoms (Supplementary Table 3). Nevertheless, the occupation ratios of vanadium and oxygen atoms are $\sim 100\%$, indicating that no vanadium vacancies and oxygen vacancies are identified in $c\text{-V}_2\text{O}_3$. To control vanadium vacancies concentration, we altered the calculation time for 0.5 h and 6 h ($0.5\text{ h-V}_d\text{-V}_2\text{O}_3$ and $6\text{ h-V}_d\text{-V}_2\text{O}_3$) respectively. The structure information of $0.5\text{ h-V}_d\text{-V}_2\text{O}_3$ and $6\text{ h-V}_d\text{-V}_2\text{O}_3$ was revealed by Rietveld refinement with combined XRD and NPD patterns. The refined results are shown in Supplementary Table 3, suggesting that the structures of $0.5\text{ h-V}_d\text{-V}_2\text{O}_3$ and $6\text{ h-V}_d\text{-V}_2\text{O}_3$ are the same as the $V_d\text{-V}_2\text{O}_3$. However, the occupation ratios of $0.5\text{ h-V}_d\text{-V}_2\text{O}_3$ and $6\text{ h-V}_d\text{-V}_2\text{O}_3$ are 97.0(4)% and 95.3(1)%, respectively, while no oxygen vacancies are found (Supplementary Figs. 9 and 10). Accordingly, it can be concluded that the $V_d\text{-V}_2\text{O}_3$, $0.5\text{ h-V}_d\text{-V}_2\text{O}_3$, and $6\text{ h-V}_d\text{-V}_2\text{O}_3$ contain 5.7%, 3.0%, and 4.7% vanadium vacancies respectively, and no oxygen vacancies are identified, while $c\text{-V}_2\text{O}_3$ has neither vanadium vacancies nor oxygen vacancies.

Electrochemical energy storage measurements. To investigate the Zn^{2+} storage performance of the $V_d\text{-V}_2\text{O}_3$ cathode, the 2032 type coin-cells were assembled using a zinc foil anode, a $3\text{ M Zn}(\text{CF}_3\text{SO}_3)_2$ electrolyte (Supplementary Figs. 11 and 12), and a filter paper separator. As shown in Supplementary Fig. 13, the cyclic voltammetry (CV) curves are carried out at a scan rate of 0.1 mV s^{-1} within a voltage window of $0.1\text{--}1.3\text{ V}$ (vs Zn/Zn^{2+}). Two pairs of redox peaks located at $1.09/0.93\text{ V}$ and $0.78/0.53\text{ V}$ are observed, which attributes to a two-step (de)intercalation process of Zn^{2+} . The rate performance at specific currents from

0.1 to 4.0 A g^{-1} is presented in Fig. 3a, b. The reversible capacities of the $\text{Zn}||\text{V}_d\text{-V}_2\text{O}_3$ cell are 196, 187, 165, 147, 138, 125, 117 and 113 mA h g^{-1} at the specific currents of 0.1, 0.3, 0.5, 0.8, 1.0, 2.0, 3.0, and 4.0 A g^{-1} , respectively. When specific current returns to 0.5 A g^{-1} , a specific capacity of 163 mA h g^{-1} is restored, thus demonstrating the electrochemical reversibility of the $\text{Zn}||\text{V}_d\text{-V}_2\text{O}_3$ cell. Furthermore, we compared the capacity retention rate of different ZIBs electrodes when the specific current was increased tenfold as shown in Supplementary Fig. 14 and Supplementary Table 4. When the specific current increases ten times, the capacity retention rate is still 70.4%, which is better than that of many ZIBs electrodes^{33–37}, exhibiting good rate capability. We also report that the $\text{Zn}||\text{V}_d\text{-V}_2\text{O}_3$ cell delivers long cycling stability with a capacity retention rate of 98% after 10,000 cycles, 90% after 20,000 cycles, and 81% after 30,000 cycles at a specific current of 5 A g^{-1} (Fig. 3c). As shown in Supplementary Fig. 15, the life span of $V_d\text{-V}_2\text{O}_3$ is preferable to most of recently reported aqueous ZIBs (Supplementary Table 5)^{38–43}. Besides, the Ragone plot showing the specific energy and power compared with other ZIBs cathodes is disclosed in Supplementary Fig. 16. The results show that at a specific power of 332.7 W kg^{-1} , the specific energy of the $\text{Zn}||\text{V}_d\text{-V}_2\text{O}_3$ cell is 110.9 Wh kg^{-1} , which is better than many reported ZIBs cathodes, such as $\text{Na}_3\text{V}_2(\text{PO}_4)_3$ ⁴⁴, $\text{Na}_{0.95}\text{MnO}_2$ ⁴⁵, $\text{FeFe}(\text{CN})_6$ ⁴⁶, CuHCF ⁴⁷, ZnHCF ¹², VS_2 ⁴⁸. These results certainly highlight the good potentials of $V_d\text{-V}_2\text{O}_3$ cathode-based Zn batteries in the field of electrochemical energy storage devices. As shown in Supplementary Figs. 17 and 18, the $0.5\text{ h-V}_d\text{-V}_2\text{O}_3$ (3.0% vanadium vacancies), $6\text{ h-V}_d\text{-V}_2\text{O}_3$ (4.7% vanadium vacancies), and $c\text{-V}_2\text{O}_3$ (no vanadium vacancies) cathodes demonstrate inadequate rate and stability electrochemical performance for aqueous ZIBs, which strongly confirms the positive effects of vanadium vacancies in $V_d\text{-V}_2\text{O}_3$ cathode and 5.7% vanadium vacancies has the most appealing electrochemical performance, especially cycle stability (Supplementary Table 6). The long cycle life of this $V_d\text{-V}_2\text{O}_3$ cathode comes ultimately from abundant vacancy clusters that attenuate the strong electrostatic interaction between Zn^{2+} and the $V_d\text{-V}_2\text{O}_3$ host.

To further understand the Zn^{2+} storage performance, the electrochemical kinetics was investigated. As shown in Fig. 3d, CV measurements are carried out at different scan rates. With the increase of scan rates from 0.1 to 1.0 mV s^{-1} , the CV curves show a similar shape, and the reduction and oxidation peaks are well preserved. Regularly, the peak currents (i) and their corresponding sweep rates (ν) obey a power-law relationship that is described by

$$i = a\nu^b, \quad (1)$$

where i represents the peak current (A), ν represents the scan rate (V s^{-1}), and a , b are constants. The b values are used as the base for analyzing electrochemical processes. As known, a b value of 0.5 indicates an electrochemical process that governed by ionic diffusion, while a b value of 1.0 indicates a capacitive storage process. From the equation of $\log(i) = b\log(\nu) + \log(a)$ derived from Eq. (1), the calculated b values for both cathode and anode peaks from CV curves are 0.94, 0.75, 0.79, and 0.88, respectively (Fig. 3e). It is suggested that the Zn^{2+} storage behavior in $V_d\text{-V}_2\text{O}_3$ is controlled collectively by ionic diffusion and capacitive processes, which leads to fast Zn^{2+} diffusion kinetics enabling the high-rate performance. In order to further quantify the contribution of diffusion-controlled and capacitive-controlled at a specific scan rate, Eq. (1) is divided into two halves to form formula (2):

$$i(V) = k_1\nu + k_2\nu^{1/2} \quad (2)$$

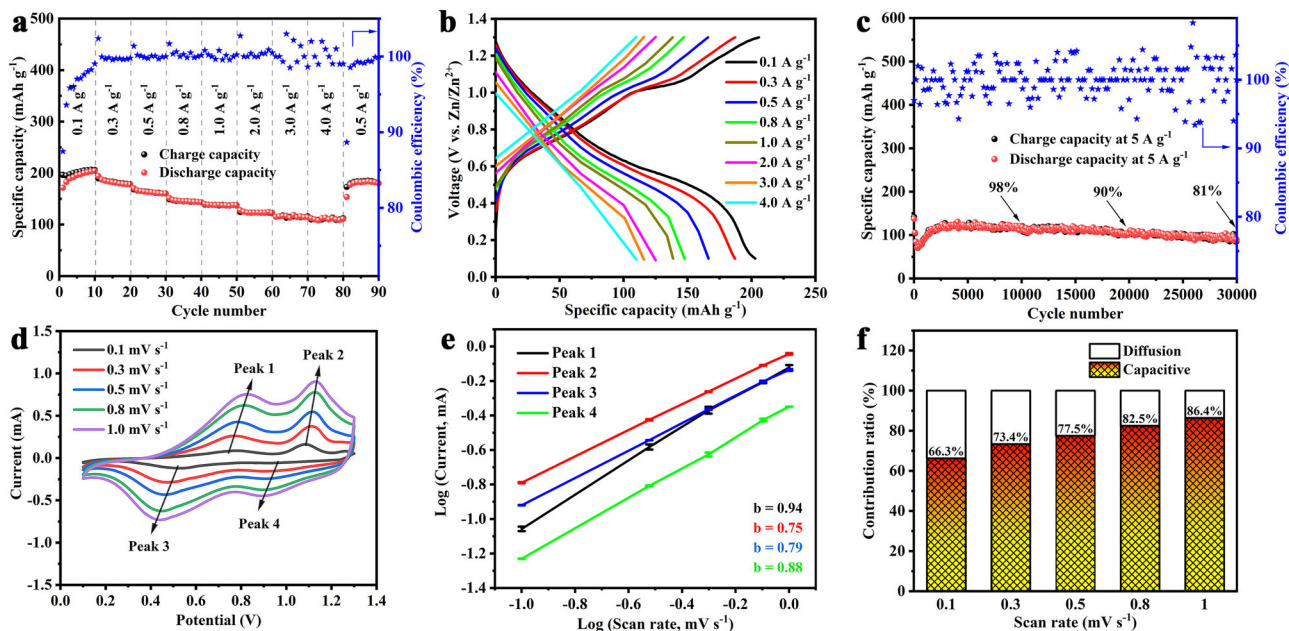


Fig. 3 Electrochemical energy storage performance of Zn||V_d-V₂O₃ cells. **a** Rate performance at different specific currents for V_d-V₂O₃. **b** Galvanostatic discharge profiles of V_d-V₂O₃ at increasing specific currents from 0.1 to 4 A g⁻¹. **c** Long-term cycling performance and coulombic efficiency for V_d-V₂O₃ at a specific current of 5 A g⁻¹. **d** CV curves of the V_d-V₂O₃ at scan rates ranging from 0.1 to 1 mV s⁻¹. **e** Error bars plot of Log (i) versus log (v) plots at specific peak currents (The R² values corresponding to the lines of peaks 1, 2, 3, and 4 are 0.9975, 0.9998, 0.9998, and 0.9995, respectively). **f** Contribution ratios of capacitive and diffusion-controlled capacities at different scan rates from 0.1 mV s⁻¹ to 1.0 mV s⁻¹.

According to the above equation, the current (i) at a specific potential (V) can be divided into a capacitance limiting effect (k_1v) and a diffusion control effect ($k_2v^{1/2}$). As shown in Supplementary Fig. 19, the capacitance contribution (corresponding to the purple region) is 82.5% of the overall contribution at a scan rate of 0.8 mV s⁻¹. With the increases of scan rates from 0.1 to 1 mV s⁻¹, the capacitance contribution rates increase from 66.3% to 86.4% (Fig. 3f). This shows that the proportion of capacitance dominated process is increased, which directly contributes to good rate performance due to the fast kinetics of Zn²⁺. Galvanostatic intermittent titration technique (GITT) is performed to analyze the diffusion coefficient of Zn²⁺ in the Zn||V_d-V₂O₃ cell (Supplementary Figs. 20 and 21). The result shows that the diffusion coefficient of Zn²⁺ in the V_d-V₂O₃ is between 10⁻⁷ and 10⁻⁸ cm² s⁻¹, which stays ahead of the other existing cathodes^{6,49,50}.

Zinc-ion storage mechanism of V_d-V₂O₃. Density functional theory (DFT) calculations were conducted to explore the function of V_d-V₂O₃ for Zn²⁺ storage. To investigate the distribution of vanadium vacancies, diverse vanadium-defective models at the concentration of 6.25%, in good agreement with the XRD and NPD Rietveld refinement results were constructed as shown in Supplementary Fig. 22. A lower formation enthalpy represents a more stable phase. Structure 1 possesses the smallest formation enthalpy, illustrating the short aggregation of V_d clusters. Then, the pristine V₂O₃ (p-V₂O₃) and V_d-V₂O₃ were implemented to disclose the insertion of Zn²⁺. The blocked insertion of Zn²⁺ into p-V₂O₃ was observed due to the positive Gibbs free energy (2.69 eV)²⁷, demonstrating almost no capacity contribution (Fig. 4a), which is consistent with the poor Zn²⁺ storage performance of c-V₂O₃ (Supplementary Fig. 18). Furthermore, the direct insertion of Zn²⁺ into p-V₂O₃ may cause structural instability. However, for V_d-V₂O₃, vanadium vacancies accept the insertion of Zn²⁺ and provide high capacity than c-V₂O₃.

Intriguingly, the distinguishing Gibbs free energies demonstrate the process of insertion of Zn²⁺ into V_d-V₂O₃ is different. Firstly, the vanadium defect is occupied with Zn²⁺ and a large amount of heat was released (-1.34 eV) due to the strong electrostatic interaction, improving the integrities and stabilities of V_d-V₂O₃. Nevertheless, due to this strong electrostatic interaction, the extraction of this kind of Zn²⁺ is unbearable, demonstrating the self-anchoring action of Zn²⁺ in the lattice. Secondly, the feasible and sustainable insertion of Zn²⁺ into V_d-V₂O₃ is observed, affording the capacity and voltage (Fig. 4a). This phenomenon may lead to the residual of Zn in V_d-V₂O₃. Consequently, the dual-effect of vanadium vacancies in V_d-V₂O₃ is specified in Fig. 4b. When Zn²⁺ initially enters into the V_d-V₂O₃ that has many vanadium vacancies, part of Zn²⁺ will be riveted on vanadium vacancies and caged inside during the whole time. It is worth noting that the coulombic efficiency of the first cycle and the second cycle was compared, which increased from 87.1% to 93.6%, indicating that the V_d-V₂O₃ indeed undergoes a self-optimization process after the first discharge. In other words, the eventual structure is a Zn doped V_d-V₂O₃ after the first discharging self-optimized process, in which the Zn²⁺ can reversibly insert or leave in the subsequent cycles.

Based on the above analysis, a series of characterizations were conducted to demonstrate the Zn²⁺ storage mechanism of the V_d-V₂O₃ cathode and the effect of vanadium vacancies. It can be seen from Fig. 5a, b that the characteristic (104) and (110) peaks move to a lower 2θ degree during the discharging process and return to the original position in the subsequent charge process. These reversible movements originate from the expansion and contraction of the lattice of V_d-V₂O₃ with the de/intercalation of Zn²⁺. Besides, no other diffraction peaks were detected, indicating no phase transformations in the V_d-V₂O₃ electrodes during the charge/discharge process. The stability of V_d-V₂O₃ was further verified via XRD measurements after 500 cycles (Supplementary Fig. 23). It is noteworthy that the morphology of the V_d-V₂O₃ electrodes have transformed into particles with a

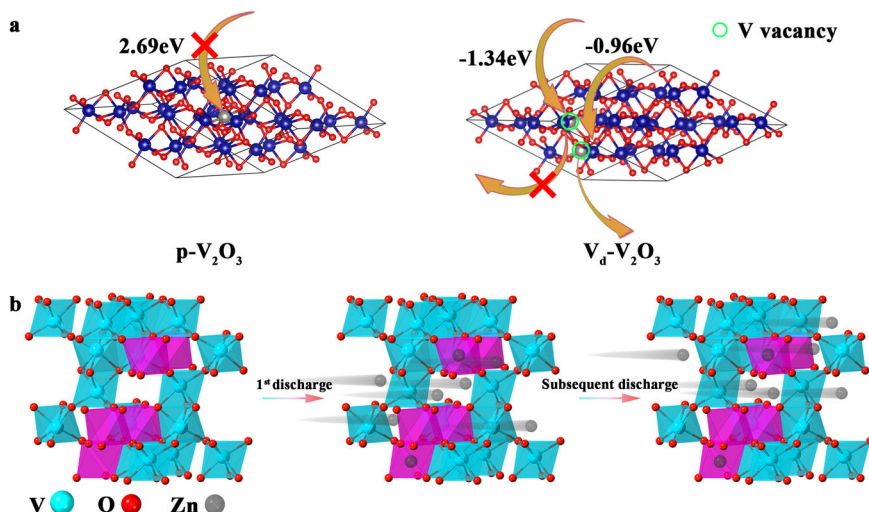


Fig. 4 Zn-ion storage mechanistic investigation in Zn||V_d-V₂O₃ cells. **a** The Gibbs free energy of different models. **b** The schematic illustration of the energy storage mechanism in the Zn||V_d-V₂O₃ cells.

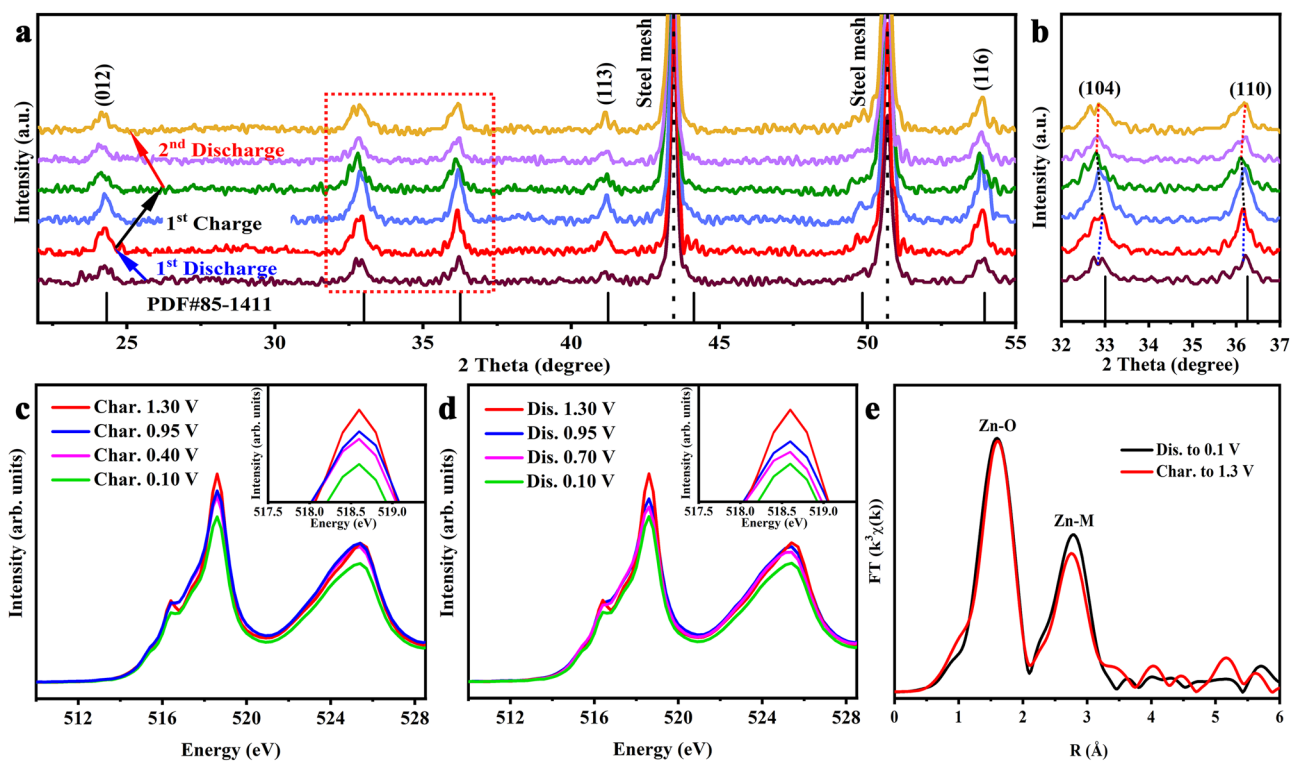


Fig. 5 Ex situ V_d-V₂O₃ electrode measurements. **a** Ex situ XRD patterns of V_d-V₂O₃ electrodes at different cut-off voltages during the charge and discharge process. **b** An enlarged view of the red dotted frame in Fig. 4a. **c** Normalized XANES spectrum of the V L-edge for V_d-V₂O₃ electrodes at different voltages during the charging process. **d** Normalized XANES spectrum of the V-edge for V_d-V₂O₃ electrodes at different voltages during the discharging process. **e** Fourier-transformed Zn K-edge EXAFS spectra of V_d-V₂O₃ electrodes at fully charged and discharged states.

diameter of ~25 nm after the first cycle and remained unchanged in the subsequent cycles, which adapts to the reversible insertion/extraction of Zn²⁺ better. (Supplementary Figs. 24–26).

XPS and soft X-ray absorption spectroscopy (sXAS) measurements were performed to give insight into the chemical states of the V_d-V₂O₃ electrodes at different states. The reversible insertion and extraction of Zn²⁺ are shown in Supplementary Fig. 27. At a fully discharged state, the V_d-V₂O₃ electrode displays two Zn 2p_{3/2} components located at 1022.5 eV and 1023.2 eV which belong to the intercalated Zn²⁺ at different

occupation sites (vanadium vacancies and tunnels nearby vanadium vacancies). At a fully charged state, the Zn 2p_{3/2} peak located at 1023.2 eV disappears while the peak of 1022.5 eV is preserved. That is to say that some vanadium vacancies occupying Zn²⁺ are riveted in the lattice of V_d-V₂O₃, only enabling Zn²⁺ reversibly (de)intercalation in the tunnel neighboring the remaining vanadium vacancies. Precise quantification of the V and Zn contents at fully dis/charged states was carried out via inductively coupled plasma emission spectroscopy (ICP-AES) measurements and the detailed results shown in

Supplementary Table 7. The results are verified via TEM elemental mapping where the Zn, V, and O elements are uniformly distributed (Supplementary Figs. 28 and 29). The charge compensation of V in the process of Zn^{2+} insertion/extraction is shown in the V L-edge patterns (Fig. 5c, d). Two peaks located at ~ 518 eV and 525 eV are observed in the V L-edge pattern, corresponding to $V 2p_{3/2} \rightarrow V 3d$ and $V 2p_{1/2} \rightarrow V 3d$ transitions, respectively^{51,52}. The intensity of V $2p_{3/2}$ peaks are increased with the entrance of Zn^{2+} and decreased with the release of Zn^{2+} , gradually, stating the electronic acquirement and deprivation of V in the Zn^{2+} electrochemistry. Notably, under the same voltage, the peak intensity remains the same revealing the high reversibility of the $\text{V}_d\text{-V}_2\text{O}_3$ electrode. The valence changes in the whole cycle are also shown in the high-resolution XPS of V (Supplementary Fig. 30) where the peak of V^{4+} becomes dominant upon charging, while releasing a sign of a let-up upon discharging. Given the local environment of vacancy, the local chemical and electronic environment of intercalated Zn^{2+} was investigated by Zn K-edge XAFS. Since the surrounding local environment of Zn^{2+} is the same during charging and discharging, the K-edge XAFS of Zn is changeless (Fig. 5e and Supplementary Fig. 31).

In summary, we have quantified 5.7% V_d clusters in a $\text{V}_d\text{-V}_2\text{O}_3$ cathode for aqueous ZIBs which shows appealing Zn^{2+} storage performance. The DFT calculations indicated that the Zn^{2+} storage reversibility and stability improved under the effects of V_d clusters. In detail, part of vanadium vacancies provides permanent sites for the preoccupation of a small amount of Zn^{2+} so that the system could pose a more stable structure to avoid deterioration during the process of Zn^{2+} insertion/extraction. Meanwhile, the other vanadium vacancies can effectively weaken the strong interaction between Zn^{2+} and the V_2O_3 material host to allow free insertion/extraction of Zn^{2+} . Benefitting from the 5.7% V_d clusters, the $\text{V}_d\text{-V}_2\text{O}_3$ cathode achieved a capacity of 196 mA h g^{-1} at 0.1 A g^{-1} , and exhibited long stability up to 30,000 cycles with a capacity retention of 81%. This accurately quantifying and determining the effect of defects opens a window for designing aqueous ZIBs cathodes with long stability.

Methods

Preparation of $\text{V}_d\text{-V}_2\text{O}_3$. The $\text{V}_d\text{-V}_2\text{O}_3$ was prepared by a hydrothermal method. First of all, 0.1856 g of vanadyl acetylacetonate and 0.42 g of urea were dissolved in 30 ml of ethylene glycol. Subsequently, 5 ml H_2O_2 (6 wt%) was poured into the above-mentioned solution and stirred evenly. After that, the obtained solution was transferred to a Teflon-lined sealed autoclave (50 ml) and kept at 200°C for 8 h. After natural cooling, the obtained precursor was washed five times with deionized water and ethanol, and then freeze-dried for further use. The freeze-dried powder was calcined at 600°C for 2 h with a heating rate of $5 \text{ min } ^\circ\text{C}^{-1}$ in argon mixed with 20% hydrogen atmosphere. After the above process, black $\text{V}_d\text{-V}_2\text{O}_3$ powder was obtained.

Materials characterizations. SEM images and TEM images were observed by a cold field SEM (SU8220) and a transmission electron microscopy (TEM: JEOL JEM2010), respectively. The chemical states were detected by EPR on a tyFA200. XPS results were obtained from electron energy dispersive spectroscopy (ESCALAB 250) with monochrome Al anode (Al K α = 1486.6 eV). The binding energy had been corrected by carbon energy of 284.6 eV. The nitrogen adsorption/desorption isotherms were obtained on a TriStar II 3020 analyzer. The TGA was performed on Q5000 at $10^\circ\text{C min}^{-1}$ under air atmosphere. Plasma Atomic Emission Spectrometer (Optima 7300 DV) was used to determine the content of elements. The V L-edge was measured at the beamline BL07W of the Hefei Synchrotron Radiation Equipment. The V K-edge was obtained on the beamline 1W1B in Beijing Synchrotron Radiation Facility (BSRF). The X-ray was monochromatized by a double-crystal Si (111) monochromator, and the energy was calibrated using a V metal foil for V K-edge. XAFS data were analyzed with the WinXAS3.1 program⁵³. The Zn K-edge was got from the beamline 14W1 of the Shanghai Synchrotron Radiation Facility (SSRF). The X-ray was monochromatized by a double-crystal Si (111) monochromator, and the energy was calibrated using a Zn metal foil for Zn K-edge. XAFS data were analyzed with the WinXAS3.1 program⁵³. Theoretical amplitudes and phase-shift functions of Zn-O and Zn-Zn were calculated with the

FEFF8.2 code⁵⁴ using the crystal structural parameters of the ZnO. XRD patterns were obtained on a Sample horizontal high-power X-ray diffractometer (Rigaku TTRIII) with Cu radiation ($\lambda = 1.54 \text{ \AA}$) in a range of $5\text{-}120^\circ$. NPD data were collected at the beamline of general purpose powder diffractometer (GPPD) at the China Spallation Neutron Source (CSNS). The XRD and NPD data were refined by the Rietveld method using the General Structure Analysis System⁵⁵ (GSAS) suite of programs with the EXPGUI⁵⁶ interface. The PALS measurements were carried out at SKLPDE (State Key Laboratory of Particle Detection and Electronics) of USTC. The PAL spectra were collected using a fast-fast coincidence system with a time resolution of around 200 ps in full width at half maximum (FWHM). The prepared sample powder was pressed into disc-shaped pellets with a diameter of 8 mm and a thickness of ~ 2 mm. A ^{22}Na positron source ($\sim 30 \mu\text{Ci}$, sealed between two Kapton films of $0.0075 \times 10 \times 10$ mm) was sandwiched between two identical pellet-shaped samples. The sample-source-sample set was fixed in a chamber that was evacuated by a turbo molecular pump. The total channel number is 4096, and the channel width is 10.417 ps/channel. The total counts of 2×10^6 were collected for each PAL spectrum. The PAL spectra were decomposed using the LTv9 software⁵⁷.

Measurements of electrochemical performance. All the electrodes used in this experiment were made by the following steps: (1) The active material of $\text{V}_d\text{-V}_2\text{O}_3$ (~ 40 mg), Ketjen Black and polyvinylidene fluoride (PVDF) were weighed at the mass ratio of 7:2:1, and then mixed and ground in an agate mortar for 15 min. (2) 250 μL *N*-methyl-2-pyrrolidone (NMP) was added into the agate mortar with further grinding for 5 min. (3) After grinding completely and uniformly, the resultant slurry was coated on the pretreated stainless steel mesh (The stainless steel mesh was pretreated as follow: first, the stainless steel mesh of 1000-mesh was punched into circles with a radius of 6 mm, then immersed in ethanol solution to ultrasonic wash for 5–10 min, and finally put it in a 100°C vacuum to dry for 12 h). The mass loading of active material on each stainless steel mesh is $\sim 1.13 \text{ mg cm}^{-2}$. (4) The coated stainless steel mesh was put into a 70°C oven for pre-drying for 30 min and then moved into a 100°C vacuum oven to dry for 12 h. The positive shell, the above-mentioned dried electrode, type 102 medium speed qualitative filter paper (separator) with a radius of 10 mm, 120 μL 3 M $\text{Zn}(\text{CF}_3\text{SO}_3)_2$ (98% pure electrolyte salt), zinc sheet (counter electrode), gasket, shrapnel, and negative shell were assembled into a CR-2032 coin-cell in above order. The metal purity of zinc sheet purchased from Chengshuo Company is not $<99.99\%$, whose radius and thickness are respectively 6 mm and 30 μm . The rate performance, stability performance, and GITT of the cells were tested in an environmental chamber under the Land CT2001A battery test system in the voltage range of 0.1–1.3 V at 25°C . The GITT curves were charged and discharged for 1 min at a specific current of 150 mA g^{-1} , then relaxed for 30 min to reach the quasi-equilibrium potential. The CV curves at different scan rates were performed on the electrochemical workstation (CHI660D, Shanghai CH Instrument Company, China) in the voltage range of 0.1–1.3 V. Before performing the ex-situ electrode measurements, the assembled cells after cycled at different cut-off voltages were disassembled in an environmental chamber at 25°C . The electrodes taken out of the cells were rinsed with ethanol 4–5 times. Afterward, the cleaned electrodes were dried in an 80°C vacuum drying oven, and then transferred to a glove box filled with argon, and taken it out before the measurements.

DFT calculation. First-principles calculations were performed by using DFT⁵⁸ based on project augmented wave method (PAW)⁵⁹ which is implemented in the Vienna ab initio Simulation Package (VASP)⁶⁰. In order to circumvent the over delocalization of the 3d-electrons in metal oxides, the DFT + *U* ($U = 3.25 \text{ eV}$) method is implemented⁶¹. Perdue-Burke-Ernzerhof (PBE)⁶² version of the generalized gradient approximation (GGA) is performed to deal with the exchange and correlation energy. The Brillouin zone is sampled by using $3 \times 3 \times 1$ based on Monkhorst-Pack k-point mesh. A plane-wave basis set with a cutoff energy of 450 eV is efficient to guarantee the convergence of the total energy. The atoms in the structure are completely relaxed with force below 0.01 eV \AA^{-1} .

Data availability

All the relevant data are included in the paper and its Supplementary Information. Source data are provided with this paper.

Received: 18 April 2021; Accepted: 9 November 2021;
Published online: 25 November 2021

References

- Larcher, D. & Tarascon, J. M. Towards greener and more sustainable batteries for electrical energy storage. *Nat. Chem.* **7**, 19–29 (2015).
- Lu, Y., Goodenough, J. B. & Kim, Y. Aqueous cathode for next-generation alkali-ion batteries. *J. Am. Chem. Soc.* **133**, 5756–5759 (2011).
- Idota, Y., Kubota, T., Matsufoji, A., Maekawa, Y. & Miyasaka, T. Tin-based amorphous oxide: a high-capacity lithium-ion-storage material. *Science* **276**, 1395–1397 (1997).

4. Bruce, P. G., Freunberger, S. A., Hardwick, L. J. & Tarascon, J. M. Li-O₂ and Li-S batteries with high energy storage. *Nat. Mater.* **11**, 19–29 (2011).
5. Goodenough, J. B. & Park, K. S. The Li-ion rechargeable battery: a perspective. *J. Am. Chem. Soc.* **135**, 1167–1176 (2013).
6. Xia, C. et al. Rechargeable aqueous zinc-ion battery based on porous framework zinc pyrovanadate intercalation cathode. *Adv. Mater.* **30**, 1705580 (2018).
7. Xia, C., Guo, J., Li, P., Zhang, X. & Alshareef, H. N. Highly stable aqueous zinc-ion storage using a layered calcium vanadium oxide bronze cathode. *Angew. Chem. Int. Ed.* **57**, 3943–3948 (2018).
8. Pu, H. U. et al. Uncovering the potential of M1-site-activated NASICON cathodes for Zn-ion batteries. *Adv. Mater.* **32**, 1907526 (2020).
9. Luo, H. et al. Anodic oxidation strategy toward structure-optimized V₂O₃ cathode via electrolyte regulation for Zn-ion storage. *ACS Nano* **14**, 7328–7337 (2020).
10. Xu, C., Li, B., Du, H. & Kang, F. Energetic zinc ion chemistry: the rechargeable zinc ion battery. *Angew. Chem. Int. Ed.* **51**, 933–935 (2012).
11. Pan, H. et al. Reversible aqueous zinc/manganese oxide energy storage from conversion reactions. *Nat. Energy* **1**, 16039 (2016).
12. Zhang, L., Chen, L., Zhou, X. & Liu, Z. Towards high-voltage aqueous metal-ion batteries beyond 1.5 V: The zinc/zinc hexacyanoferrate system. *Adv. Energy Mater.* **5**, 1400930 (2015).
13. Yoo, H. D. et al. Fast kinetics of magnesium monochloride cations in interlayer-expanded titanium disulfide for magnesium rechargeable batteries. *Nat. Commun.* **8**, 339 (2017).
14. Koketsu, T. et al. Reversible magnesium and aluminium ions insertion in cation-deficient anatase TiO₂. *Nat. Mater.* **16**, 1142–1148 (2017).
15. Sun, X., Bonnicksen, P. & Nazar, L. F. Layered TiS₂ positive electrode for Mg batteries. *ACS Energy Lett.* **1**, 297–301 (2016).
16. Liao, M. et al. A deep-cycle aqueous zinc-ion battery containing an oxygen-deficient vanadium oxide cathode. *Angew. Chem. Int. Ed.* **59**, 2273–2278 (2020).
17. Hammond, C. & Hammond, C. *The Basics Of Crystallography And Diffraction*. Vol. 214 (Oxford, 2001).
18. IUPAC. Manual of symbols and terminology. *Pure Appl. Chem.* **31**, 578 (1972).
19. Wang, Q., Zhang, Y., Zheng, J., Hu, T. & Meng, C. Synthesis, structure, optical and magnetic properties of interlamellar decoration of magadiite using vanadium oxide species. *Microporous Mesoporous Mater.* **244**, 264–277 (2017).
20. Adamski, A., Spalek, T. & Sojka, Z. Application of EPR spectroscopy for elucidation of vanadium speciation in VOx/ZrO₂ catalysts subject to redox treatment. *Res. Chem. Intermed.* **29**, 793–804 (2003).
21. Yu, M. et al. Valence-optimized vanadium oxide supercapacitor electrodes exhibit ultrahigh capacitance and super-long cyclic durability of 100,000 cycles. *Adv. Funct. Mater.* **25**, 3534–3540 (2015).
22. Gou, W. et al. Yolk-shell structured V₂O₃ microspheres wrapped in N, S co-doped carbon as pea-pod nanofibers for high-capacity lithium ion batteries. *Chem. Eng. J.* **374**, 545–553 (2019).
23. Chen, S. et al. Advances in antioxidation coating materials for carbon/carbon composites. *J. Alloy. Compd.* **886**, 161143 (2021).
24. Wong, J., Lytle, F. W., Messmer, R. P. & Maylotte, D. H. K-edge absorption spectra of selected vanadium compounds. *Phys. Rev. B* **30**, 5596–5610 (1984).
25. Zhao, Y. et al. Ultrafine NiO nanosheets stabilized by TiO₂ from monolayer NiTi-LDH precursors: An active water oxidation electrocatalyst. *J. Am. Chem. Soc.* **138**, 6517–6524 (2016).
26. Zhang, R. et al. Engineering cobalt defects in cobalt oxide for highly efficient electrocatalytic oxygen evolution. *ACS Catal.* **8**, 3803–3811 (2018).
27. Zhu, C. et al. Electrochemically induced cationic defect in MnO intercalation cathode for aqueous zinc-ion battery. *Energy Storage Mater.* **24**, 394–401 (2020).
28. Jean, J. Y., Mallon, P. E. & Schrader, D. M. *Principles And Applications Of Positron And Positronium Chemistry* (World Scientific, 2003).
29. Staab, T. E. M., Krause-Rehberg, R. & Kieback, B. Review Positron annihilation in fine-grained materials and fine powders—an application to the sintering of metal powders. *J. Mater. Sci.* **34**, 3833–3851 (1999).
30. Liu, Y. et al. Heterogeneous spin states in ultrathin nanosheets induce subtle lattice distortion to trigger efficient hydrogen evolution. *J. Am. Chem. Soc.* **138**, 5087–5092 (2016).
31. Liu, X., Zhou, K., Wang, L., Wang, B. & Li, Y. Oxygen vacancy clusters promoting reducibility and activity of ceria nanorods. *J. Am. Chem. Soc.* **131**, 3140–3141 (2009).
32. Noguchi, M., Kimizuka, N., Chiba, T. & Tsuda, N. Lifetime spectra of positrons in V₂O₃. *J. Phys. Soc. Jpn* **31**, 661–665 (1973).
33. Wei, S. et al. Manganese buffer induced high-performance disordered MnVO cathodes in zinc batteries. *Energy Environ. Sci.* **14**, 3954–3964 (2021).
34. Xiong, T. et al. Defect engineering of oxygen-deficient manganese oxide to achieve high-performing aqueous zinc ion battery. *Adv. Energy Mater.* **9**, 1803815 (2019).
35. Hu, P. et al. Highly durable Na₂V₆O₁₆·1.63H₂O nanowire cathode for aqueous zinc-ion battery. *Nano Lett.* **18**, 1758–1763 (2018).
36. Geng, H. et al. Electronic structure regulation of layered vanadium oxide via interlayer doping strategy toward superior high-rate and low-temperature zinc-ion batteries. *Adv. Funct. Mater.* **30**, 1907684 (2019).
37. Yang, W. et al. 3D oxygen-defective potassium vanadate/carbon nanoribbon networks as high-performance cathodes for aqueous zinc-ion batteries. *Small Methods* **4**, 1900670 (2019).
38. Wan, F. et al. Aqueous rechargeable zinc/sodium vanadate batteries with enhanced performance from simultaneous insertion of dual carriers. *Nat. Commun.* **9**, 1656 (2018).
39. He, P. et al. Sodium ion stabilized vanadium oxide nanowire cathode for high-performance zinc-ion batteries. *Adv. Energy Mater.* **8**, 1702463 (2018).
40. Li, Z. et al. Mechanistic insight into the electrochemical performance of Zn/VO₂ batteries with an aqueous ZnSO₄ electrolyte. *Adv. Energy Mater.* **9**, 1900237 (2019).
41. Zhang, N. et al. Rechargeable aqueous Zn–V₂O₅ battery with high energy density and long cycle life. *ACS Energy Lett.* **3**, 1366–1372 (2018).
42. Kundu, D., Adams, B. D., Duffort, V., Vajargah, S. H. & Nazar, L. F. A high-capacity and long-life aqueous rechargeable zinc battery using a metal oxide intercalation cathode. *Nat. Energy* **1**, 16119 (2016).
43. Liu, C. et al. Expanded hydrated vanadate for high-performance aqueous zinc-ion batteries. *Energy Environ. Sci.* **12**, 2273–2285 (2019).
44. Li, G. et al. Towards polyvalent ion batteries: a zinc-ion battery based on NASICON structured Na₃V₂(PO₄)₃. *Nano Energy* **25**, 211–217 (2016).
45. Zhang, B. et al. An aqueous rechargeable battery based on zinc anode and Na_{0.95}MnO₂. *Chem. Commun.* **50**, 1209–1211 (2014).
46. Liu, Z., Bertram, P. & Endres, F. Bio-degradable zinc-ion battery based on a prussian blue analogue cathode and a bio-ionic liquid-based electrolyte. *J. Solid State Electrochem.* **21**, 2021–2027 (2017).
47. Trocoli, R. & La Mantia, F. An aqueous zinc-ion battery based on copper hexacyanoferrate. *ChemSusChem* **8**, 481–485 (2015).
48. He, P. et al. Layered VS₂ nanosheet-based aqueous Zn ion battery cathode. *Adv. Energy Mater.* **7**, 1601920 (2017).
49. Yang, Y. et al. Li⁺ intercalated V₂O₅·nH₂O with enlarged layer spacing and fast ion diffusion as an aqueous zinc-ion battery cathode. *Energy Environ. Sci.* **11**, 3157–3162 (2018).
50. Fang, G. et al. Suppressing manganese dissolution in potassium manganate with rich oxygen defects engaged high-energy-density and durable aqueous zinc-ion battery. *Adv. Funct. Mater.* **29**, 1808375 (2019).
51. Goering, E., Müller, O., Klemm, M., denBoer, M. L. & Horn, S. Angle dependent soft-X-ray absorption spectroscopy of V₂O₅. *Philos. Mag. B* **75**, 229–236 (2006).
52. Velazquez, J. M., Jaye, C., Fischer, D. A. & Banerjee, S. Near edge X-ray absorption fine structure spectroscopy studies of single-crystalline V₂O₅ nanowire arrays. *J. Phys. Chem. C* **113**, 7639–7645 (2009).
53. Ressler, T. WinXAS- A program for X-ray absorption spectroscopy data. *J. Synchrotron Radiat.* **5**, 118–122 (1998).
54. Ankudinov, A. L., Ravel, B., Rehr, J. J. & Conradson, S. D. Real-space multiple-scattering calculation and interpretation. *Phys. Rev. B* **58**, 7565–7576 (1998).
55. Larson A. C. & Von Dreele R. B. *General Structure Analysis System (GSAS). Los Alamos National Laboratory Report LAUR 86-748* (1994).
56. Toby, B. EXPGUI, a graphical user interface for GSAS. *J. Appl. Crystallogr.* **34**, 210–213 (2001).
57. Kinsky, J. Microcomputer program for analysis of positron annihilation lifetime spectra. *Nucl. Instrum. Methods Phys. Res. A* **374**, 235–244 (1996).
58. Kohn, W. & Sham, L. J. Self-consistent equations including exchange and correlation effects. *Phys. Rev.* **140**, A1133–A1138 (1965).
59. Blochl, P. E. Projector augmented-wave method. *Phys. Rev. B* **50**, 17953–17979 (1994).
60. Zhu, K., Wu, T. & Huang, K. A high capacity bilayer cathode for aqueous Zn-ion batteries. *ACS Nano* **13**, 14447–14458 (2019).
61. Kresse, G. & Furthmüller, J. Efficient iterative schemes for *ab initio* total-energy calculations using a plane-wave basis set. *Phys. Rev. B* **54**, 11169–11186 (1996).
62. Perdew, J. P., Burke, K. & Ernzerhof, M. Generalized gradient approximation made simple. *Phys. Rev. Lett.* **77**, 3865–3868 (1996).

Acknowledgements

This work was financially supported in part by the National Key R&D Program of China (2020YFA0405800-L.S.), NSFC (U1932201-L.S., U2032113-S.M.C., and 22075264-S.M.C.), CAS Collaborative Innovation Program of Hefei Science Center (2019HSC-CIP002-S.L., 2020HSC-CIP002-S.M.C.), CAS International Partnership Program

(211134KYSB20190063-S.L.), and USTC Research Funds of the Double First-Class Initiative (Grant No. YD2310002003-S.M.C.). L.S. acknowledges the support from Institute of Energy, Hefei Comprehensive National Science Center, University Synergy Innovation Program of Anhui Province (GXXT-2020-002). The authors thank the Beijing Synchrotron Radiation Facility (1W1B, 4W1B and 4B9A, BSRF), Shanghai Synchrotron Radiation Facility (BL14W1 and 14B1, SSRF), the Hefei Synchrotron Radiation Facility (MCD-A and MCD-B Soochow Beamline for Energy Materials, Infrared spectroscopy and microspectroscopy at NSRL), and the USTC Center for Micro and Nanoscale Research and Fabrication for helps in characterizations.

Author contributions

L.S. and S.M.C. supervised the project. K.F.Z. and S.Q.W. designed the work and carried out most of the experiments. L.H.H. and F.R.S. measured and analyzed XRD and NPD data. H.W.S. simulated most of the calculations. P.J.Z. and C.D.W. performed XAFS and sXAS experiments. Y.Y.C. and X.G. helped to prepare most of the samples. H.J.Z., B.J.Y., and M.L. guided the PALS measurements and helped to analyze PALS results. X.J.W. helped to explain some experimental data. All the authors discussed the results and assisted during the manuscript preparation.

Competing interests

The authors declare no competing interests.

Additional information

Supplementary information The online version contains supplementary material available at <https://doi.org/10.1038/s41467-021-27203-w>.

Correspondence and requests for materials should be addressed to Shuangming Chen, Lunhua He or Li Song.

Peer review information *Nature Communications* thanks Nasr Bensalah, Kothandaraman ramanujam, and the other, anonymous, reviewer(s) for their contribution to the peer review of this work. Peer reviewer reports are available.

Reprints and permission information is available at <http://www.nature.com/reprints>

Publisher's note Springer Nature remains neutral with regard to jurisdictional claims in published maps and institutional affiliations.



Open Access This article is licensed under a Creative Commons Attribution 4.0 International License, which permits use, sharing, adaptation, distribution and reproduction in any medium or format, as long as you give appropriate credit to the original author(s) and the source, provide a link to the Creative Commons license, and indicate if changes were made. The images or other third party material in this article are included in the article's Creative Commons license, unless indicated otherwise in a credit line to the material. If material is not included in the article's Creative Commons license and your intended use is not permitted by statutory regulation or exceeds the permitted use, you will need to obtain permission directly from the copyright holder. To view a copy of this license, visit <http://creativecommons.org/licenses/by/4.0/>.

© The Author(s) 2021